Impurity toroidal rotation and transport in Alcator C-Mod ohmic h-mode plasmas

J. E. Rice, J. A. Goetz, R. S. Granetz, M. J. Greenwald,
A. E. Hubbard, I. H. Hutchinson, E. S. Marmar, D. Mossessian,
T. Sunn Pedersen, J. A. Snipes, J. L. Terry and S. M. Wolfe

Plasma Science and Fusion Center, Massachusetts Institute of Technology

175 Albany St., Cambridge, MA 02139-4307

Abstract

Central toroidal rotation and impurity transport coefficients have been determined in Alcator C-Mod Ohmic High Confinement Mode (H-mode) plasmas from observations of x-ray emission following impurity injection. Rotation velocities up to 3×10^4 m/s in the co-current direction have been observed in the center of the best Ohmic H-mode plasmas. Purely Ohmic H-mode plasmas display many characteristics similar to Ion Cyclotron Range of Frequencies (ICRF) heated H-mode plasmas, including the scaling of the rotation velocity with plasma parameters and the formation of edge pedestals in the electron density and temperature profiles. Very long impurity confinement times ($\sim$1 s) are seen in Edge Localized Mode-free (ELM-free) Ohmic H-modes and the inward impurity convection velocity profile has been determined to be close to the calculated neo-classical profile.

I. Introduction

Plasma rotation plays an important role in the transition from Low Confinement Mode (L-mode) to High Confinement Mode (H-mode) in tokamak plasmas [1-4], and is associated with the formation of transport barriers. Most observations of toroidal rotation [5 and references therein] have been made in plasmas with an external momentum source, usually provided by neutral beams. It is difficult to separate the contribution to the rotation from the direct momentum input of the neutral beams and the rotation that may be associated with (or induced by) H-modes. ICRF-only heated discharges provide the opportunity for the study of toroidal rotation in plasmas with no direct momentum input - co-current rotation in ICRF-only plasmas [6-9] has been documented - but since there exist some ICRF drive mechanisms [10-15], the intrinsic association between rotation and H-mode is still ambiguous. The rotation observed in Ohmic H-modes [16,17,8,9,18] provides an unequivocal demonstration of the connection between H-modes and co-current toroidal rotation. Toroidal impurity rotation on the magnetic axis in Ohmic L-mode plasmas (also with no net momentum input) is consistent with neoclassical predictions [19-21] where the rotation is driven by the parallel electric field and friction with the electrons; in Ohmic L-mode discharges, impurities rotate in the direction opposite to the plasma current [22,23,19,20].

Comparison of observations of impurity toroidal rotation in plasmas with no direct momentum input [9] has been made with calculations from neo-classical theory [21], which predicts the rotation to be inversely proportional to the poloidal magnetic field, with three terms, depending on the ion density gradient, the ion temperature gradient and the radial electric field. While it's true that during H-modes the density and temperature gradients substantially increase, this would give rise to a large toroidal rotation only at the plasma edge, and in order to explain the central rotation, the presence of a substantial positive core radial electric is inferred. In the treatment of Ref.[21], the radial electric field is not calculated from first principles. E_r is determined self-consistently in the sub-neo-classical theory

[24], but only near the plasma boundary.

Impurity confinement in tokamak plasmas has been studied extensively [25 and references therein]. Impurity transport in Ohmic L-mode plasmas is generally characterized as anomalous [26-32], with diffusion coefficients ranging from 100-1000 times larger than neo-classical predictions [33]. In neutral beam and ICRF H-mode plasmas, longer impurity confinement is observed, characterized by a large edge inward convection velocity [34-39], similar to neo-classical predictions. There are few direct measurements of impurity transport in Ohmic H-mode plasmas, other than some documented increases in the global $Z_{\rm eff}$.

Ohmic H-modes have been observed on DIII-D [16], ASDEX Upgrade [40], Alcator C-Mod [41], COMPASS-C [17] and TCV [42]. These are achieved by exceeding the H-mode threshold [40], which for Ohmic discharges usually means operating at higher plasma current (to increase the input power) and at low density and toroidal magnetic field (to lower the threshold). These H-modes are typically not as robust as those obtained with auxiliary heating (mainly because with only Ohmic input power, the plasmas are barely above the H-mode threshold), but do exhibit characteristics similar to other H-modes, such as the formation of steep edge pedestals, and improved energy, particle and impurity confinement.

The outline of this paper is as follows: an experimental description and the observations of toroidal rotation, including scalings with stored energy and plasma current are presented in Section II, edge pedestals, observations of impurity confinement and impurity transport coefficients are discussed in Section III and conclusions are drawn in Section IV.

II. Experiment Description and Observations of Toroidal Rotation

The observations presented here were obtained from the Alcator C-Mod [43] tokamak, a compact (major radius R = 0.67 m, typical minor radius of 0.22 m, and elongation $\kappa \leq 1.8$), high field device ($2.6 \leq B_T \leq 7.9$ T) in the lower single null configuration, which has operated with plasma currents between 0.23 and 1.5 MA and volume averaged electron densities between 0.24 and 5.9 $\times 10^{20}/m^3$. Rotation velocities have been determined from the Doppler shifts of the Ar^{17+} Lyman α doublet [44,45] (1s $^1S_{\frac{1}{2}}$ - 2p $^2P_{\frac{3}{2}}$ at 3731.10 mÅ, and 1s $^1S_{\frac{1}{2}}$ - 2p $^2P_{\frac{1}{2}}$ at 3736.52 mÅ). For the central temperature range of Alcator C-Mod, hydrogenlike argon is a core charge state. X-ray spectra are measured with a tangentially viewing von Hamos type spectrometer [46] and an array of five nearly-radially viewing, spatially scannable von Hamos type spectrometers [47]. Spectra are typically collected every 20 ms during plasma discharges, and averaged over sawtooth oscillations which are normally present. Argon is routinely injected into Alcator C-Mod plasmas through a piezoelectric valve, to provide x-ray transitions for Doppler width ion temperature measurements. Absolute wavelength calibration for the tangential spectrometer was obtained from the potassium K_α lines generated from a KCl fluorescence x-ray source [45].

Shown in Fig.1 are the time histories of several parameters of interest for an Ohmic H-mode plasma. This H-mode was achieved by operating at relatively high plasma current (1.1 MA), in order to increase the total input power, and by ramping down the toroidal magnetic field from 5.4 to 4.3 T, in order to lower the H-mode threshold, which has been determined to scale as B_T [40]. This plasma entered H-mode at 0.82 s, when the D_α signal dropped, and the plasma stored energy, the electron density (and temperature) and the central rotation velocity all increased. During the H-mode period, the plasma stored energy nearly doubled, reaching 105 kJ, the central electron density also doubled, increasing to $4.2\times 10^{20}/m^3$, while the central toroidal rotation velocity exceeded 3×10^4 m/s. Here, a positive rotation velocity indicates co-current rotation.

Similar rotation velocities have been determined from the pre- and post-cursors to sawtooth oscillations observed from magnetic pick-up coils [18], which is presumed to be indicative of the rotation velocity at the q=1 surface, as shown in Fig.2, for another Ohmic H-mode discharge. In the top frame of Fig.2 is the time evolution of the spectral intensity of sawtooth postcursors which rotate in the co-current direction during the H-mode phase; the spectral intensity has a maximum at about 8 kHz (at 0.7 s for example), which corresponds to a toroidal velocity of around 35 km/s for the 4.2 m circumference of Alcator C-Mod. This velocity agrees very well with that obtained from the x-ray Doppler shifts, also shown in the Figure. From both measurements the rotation was near zero or slightly negative (in the counter-current direction) during the L-mode phase, and changed to the co-current direction after the plasma entered H-mode. This plasma reverted briefly to L-mode twice during the H-mode period from 0.57 to 0.94 s. The plasma stored energy and the rotation velocities both decreased accordingly, but with the rotation decrease delayed by about an energy confinement time. The time histories from both rotation velocity measurements are very similar. Since there is unequivocally no external momentum input in an Ohmic plasma, the co-current rotation is strictly a feature of the H-mode transport.

There are several similarities between the observed central toroidal rotation during Ohmic and ICRF H-modes; most notable is the association of the rotation velocity and the plasma stored energy, which is apparent from Figs.1 and 2. Shown in Fig.3 is the central impurity toroidal rotation velocity increase (the difference between the H-mode and pre-H-mode value) as a function of the stored energy increase for Ohmic H-mode discharges, and there is a general correlation [18], similar to the ICRF H-mode case [8,9]. These points seem to separate according to plasma current, with the rotation higher for the same stored energy increase at lower current, which is also seen during ICRF H-modes [9]. This point is emphasized in Fig.4, which shows the data points of Fig.3 with the stored energy normalized to the plasma current; the scatter is reduced considerably. Both of these trends are consistent with the predictions of the neo-classical theory of impurity rotation [21]. The impurity toroidal rotation velocity is calculated to increase with ∇P, which itself is observed to increase in conjunction with the plasma stored energy. The rotation velocity is also predicted to decrease as $1/B_P$ which agrees qualitatively with the observed decrease with I_P. However, a substantial core E_r ($\sim 10^4$ V/m) is necessary to explain the observed central toroidal rotation and a more satisfactory quantitative comparison would require a first principles calculation of E_r.

III. Edge Pedestals and Impurity Transport Coefficients

There has recently been an emphasis on edge 'pedestal' diagnostics with fine ($\sim$ 1 mm) spatial resolution on Alcator C-Mod. In particular, an edge Thomson scattering system [48], two edge x-ray cameras [49] and a visible *bremsstrahlung* system have been implemented. The formation of steep gradients in the edge electron temperature, electron density and x-ray emissivity profiles during ICRF H-modes is well documented [50,51]. Similar steep edge profiles are observed during Ohmic H-modes; the electron density and temperature profiles for the discharge of Fig.1 are shown in Fig.5. The L-mode profiles (0.75 s) are nearly linearly decreasing with radius near the plasma boundary; the position of the last closed flux surface (LCFS) is shown by the dotted vertical line. In contrast, the H-mode profiles (1.05 s) show steep pedestal formation about 5 mm inside the LCFS. The electron density profiles shown in this Figure were determined from visible *bremsstrahlung* emission. Visible continuum profiles are measured with a 2048 element 1-D charge coupled device (CCD) array, which images emission from the plasma in a passband at 536 ± 3 nm. The emission is dominated by free-free *bremsstrahlung* for $T_e > 20$ eV, which in turn is most sensitive to the electron density ($\propto n_e^2$). The toroidal mid-plane views are abel-inverted to yield local emissivity profiles, with chordal resolution in the edge pedestal region of 0.6 mm, and time resolution of 4 ms. Correcting for the weak temperature dependence using measured profiles from electron cyclotron emission, and assuming $Z_{\rm eff}$ is constant across the profile, the emissivity data are converted to equivalent electron density. The electron temperature profiles were measured by the edge Thomson scattering system. Enhanced D_α (EDA) H-modes have also been observed during Ohmic discharges [52] indicating that this particular variety of H-mode is a function of the Alcator C-Mod geometry and/or operating space, and not a unique feature of ICRF heating.

Impurity confinement times have been determined from the time histories of the emission from heliumlike calcium, Ca^{18+}, measured by the x-ray spectrometer array, following injection of CaF_2 by a laser blow-off system [53]. Shown in Fig.6 is a Ca^{18+} x-ray spectrum [54] obtained along a centrally viewing chord during a CaF_2 injection into an Ohmic L-mode discharge, when the central electron density was 1.5×10^{20} m^{-3} and the central electron temperature was 1650 eV. This spectrum is dominated by the resonance line, w (1s2p $^1P_1$ -1s^2 $^1S_0$, 3177.26 mÅ), and the forbidden line, z (1s2p $^3S_1$ -1s^2 $^1S_0$, 3211.13 mÅ) and the intercombination lines, x and y (1s2p $^3P_2$ -1s^2 $^1S_0$, 3189.19 mÅ, and 1s2p $^3P_1$ -1s^2 $^1S_0$, 3192.82 mÅ) are prominent. Also visible are several weaker satellite lines, denoted by t, q, r, k, j and 3. Shown by the thin line in the figure is a synthetic spectrum whose line intensities are equal to the calculated central chord brightnesses, line widths are given the appropriate Doppler broadening for the ion temperature and instrumental resolution and line wavelengths are taken from Refs.[55,56]. (The satellite lines have been shifted in wavelength by 1.0 mÅ, since relativistic effects were not included in these calculations.) Chordal brightnesses of w, x, y and z were determined from emissivity profiles calculated from the collisional-radiative model of Refs.[57,58], which includes population of the upper levels via collisional excitation of heliumlike Ca^{18+}, radiative recombination of hydrogenlike Ca^{19+} and inner shell ionization of lithiumlike Ca^{17+}. Emissivity profiles for the satellites have been calculated using the dielectronic satellite intensity factors from Ref.[56] and the inner shell excitation rates from Ref.[59]. Measured electron density profiles were obtained from a two color laser interferometer [60], Thomson scattering, the visible *bremsstrahlung* and reflectometer diagnostics and the electron temperature profiles were from the electron cyclotron emission and Thomson scattering diagnostics. Calcium charge state density profiles were calculated from the Multiple Ionization State Transport (MIST) code [61], using impurity transport coefficients [39] appropriate for the discharge, which will be discussed next. The agreement between the measured and simulated spectra is very good, validating the modelling of the line emission to be used in what follows.

Time histories of these calcium lines following a CaF_2 injection into the discharge presented in Fig.1 are shown in Fig.7. The asterisks depict the total of all of the calcium lines in each spectrum integrated over 50 ms bins while the thin solid line is the sum of all counts in the detector in each millisecond, which includes some background radiation. The injection occured at 0.75 s, when the plasma was still in L-mode. The x-ray signal has a very steep rise and rapid fall, characteristic of anomalous impurity transport and an impurity confinement time of about 25 ms. Shown in the Figure by the thick solid line is the simulated signal, calculated as described above, on a fine time grid, using L-mode impurity transport coefficient profiles [39], with a diffusion coefficient of 0.5 m^2/s over most of the plasma, decreasing somewhat near the edge, and with no convection velocity. At 0.82 s the plasma entered ELM-free Ohmic H-mode, with the abrupt formation of edge pedestals (Fig.5). During this H-mode interval, the impurity confinement time was very long ($\geq$1 s), characterized by reduced diffusion and with the appearance of a large inward convection velocity near the plasma edge [39]. The simulated signal with these H-mode impurity transport coefficient profiles is shown by the thick dash-dot-dot-dot line in the Figure, reflecting the observed stagnant impurity confinement. The impurity transport coefficient profiles used for the simulation during the ELM-free portion of the discharge are shown in Fig.8 (solid lines), along with the calculated neo-classical [33] (dash-dot-dot-dot lines) profiles. Here it has been assumed that the ion (not measured) and electron density and temperature profiles are the same. The anomalous diffusion coefficient profile used in the simulation is much larger than the calculated neo-classical profile over most of the plasma radius, but the values are similar near the periphery; the convection velocity profile used in the simulation is nearly identical to the calculated neo-classical profile over the entire plasma radius. The shape of the neo-classical (inward) convection velocity profile is dominated by the density profile gradient (Fig.5). When the plasma goes from L-mode to ELM-free Ohmic H-mode, whatever processes are responsible for the anomalous impurity transport are suppressed, and the convection velocity profile approaches the theoretical neo-classical one. The appearance of this very strong impurity transport 'barrier' at the plasma edge prevents the injected impurities from leaving the plasma, and gives rise to the very long confinement time.

Another manifestation of this strong neo-classical impurity pinch at the plasma periphery is apparent in the pedestal of the edge x-ray emission. Shown in Fig.9 is the x-ray emissivity profile just inside the LCFS during the Ohmic H-mode of Fig.1, which features an abrupt ∼3 mm pedestal width, located inside the density pedestal (also shown). The x-ray emissivity has been modelled assuming it is due to radiative recombination of fully stripped fluorine (F^{9+}). Ignoring the weak electron temperature dependence of radiative recombination, the x-ray emissivity is then simply proportional to the product of the electron density profile (which is measured) and the F^{9+} density profile, calculated from MIST, using the the computed neo-classical convection velocity profile for fluorine, similar to that shown in Fig.8. This calculated x-ray profile is shown by the solid line in Fig.9, and the agreement is embarassingly good. The use of the neo-classical inward convection has produced good agreement with the Ca^{18+} brightness time history and the edge F^{9+} x-ray emissivity profile.

IV. Conclusions

Substantial co-current toroidal rotation, with velocities over 3×10^4 m/s, has been observed in the core of Alcator C-Mod Ohmic H-mode plasmas which had no external momentum input. Rotation velocities deduced from the Doppler shifts of x-ray impurity emission are the same as those determined from the propagation of sawtooth pre- and post-cursors. The observed rotation velocity increases with plasma stored energy and decreases with plasma current, very similar to the scalings seen in ICRF H-modes. Ohmic H-modes have many characteristics similar to ICRF H-modes, including the formation of edge density and temperature pedestals. Ohmic EDA H-modes have also been seen, indicating that this particular variety of H-mode is a function of the Alcator C-Mod geometry and/or operating space, and not a unique feature of ICRF heating. Very long impurity confinement times (∼1

s) are observed in Ohmic ELM-free H-modes. Modelling indicates that for these plasmas, the inward impurity convection velocity is very close to the calculated neo-classical profile, very steep at the plasma periphery, approaching 100 m/s. This edge impurity transport barrier leads to a very long impurity confinement time and a steep edge x-ray emissivity pedestal, displaced inward with respect to the separatrix.

V. Acknowledgements

The authors thank J. Irby for electron density measurements, C. Fiore for ion temperature measurements and the Alcator C-Mod operations group for expert running of the tokamak. Work supported at the Massachusetts Institute of Technology by United States Department of Energy Contract No. DE-FC02-99ER54512.

References

[1] K.C. Shaing and E.C. Crume, Phys. Rev. Lett. **63** (1989) 2369.

[2] K.H. Burrell, M.E. Austin, T.N. Carlstrom et al., in *Plasma Physics and Controlled Nuclear Fusion Research 1994* Proceedings of the 15th International Conference, Seville, Spain, Vol.1 (IAEA, Vienna 1996) 221.

[3] P.H. Diamond, V.B. Lebedev, Y.M. Liang et al., in *Plasma Physics and Controlled Nuclear Fusion Research 1994* Proceedings of the 15th International Conference, Seville, Spain, Vol.3 (IAEA, Vienna 1996) 323.

[4] R.A. Moyer, K.H. Burrell, T.N. Carlstrom et al., Phys. Plasmas **2** (1995) 2397.

[5] K.H. Burrell, R.J. Groebner, H. St.John and R.P. Seraydarian, Nucl. Fusion **28** (1988) 3.

[6] L.-G. Eriksson, R. Giannella, T. Hellsten, E. Källne and G. Sundström, Plasma Phys. Contr. Fusion **34** (1992) 863.

[7] L.-G. Eriksson, E.Righi and K.D. Zastrow, Plasma Phys. Contr. Fusion **39** (1997) 27.

[8] J.E. Rice, M. Greenwald, I.H. Hutchinson et al., Nucl. Fusion **38** (1998) 75.

[9] J.E. Rice, P.T. Bonoli, J.A. Goetz et al., Nucl. Fusion **39** (1999) 1175.

[10] L. Chen, J. Vaclavik and G.W. Hammett, Nucl. Fusion **28** (1988) 389.

[11] C.S. Chang, J.Y. Lee and H. Weitzner, Phys. Fluids B **3** (1991) 3429.

[12] T. Hellsten, J. Carlsson, L.-G. Eriksson et al., in *Plasma Physics and Controlled Nuclear Fusion Research 1998* Proceedings of the 17th International Conference, Yokohama, IAEA-F1-CN-69/THP2/36.

[13] B. Coppi, G. Penn, L. Sugiyama and W. Park, in *Plasma Physics and Controlled Nuclear Fusion Research 1998* Proceedings of the 17th International Conference, Yokohama, IAEA-F1-CN-69/TH3/7.

[14] C.S. Chang, C.K. Phillips, R. White et al., in *Plasma Physics and Controlled Nuclear Fusion Research 1998* Proceedings of the 17th International Conference, Yokohama, IAEA-F1-CN-69/THP2/34.

[15] C.S. Chang, C.K. Phillips, R. White et al., Phys. Plasmas **6** (1999) 1969.

[16] T.H. Osborne, N.H. Brooks, K.H. Burrell, *et al.*, Nucl. Fusion **30**, (1990) 2023.

[17] I.H. Coffey, R. Barnsley, F.P. Keenan et al., in Proceedings of the 11th Colloquium on UV and X-ray Spectroscopy of Astrophysical and Laboratory Plasmas, Nagoya, Japan, 1995, p.431, Frontiers Science Series No.15 (Editors: K. Yamashita and T. Watanabe), Universal Academy Press, Tokyo, Japan, 1996

[18] I.H. Hutchinson, J.E. Rice, R.S. Granetz and J.A. Snipes, submitted to Phys. Rev. Lett. (1999).

[19] W.A.Peebles, D.L. Brower, R. Philipona et al., in *Plasma Physics and Controlled Nuclear Fusion Research 1990* Proceedings of the 13th International Conference, Washington D.C., Vol.1 (IAEA, Vienna 1991) 589.

[20] J.E. Rice, E.S. Marmar, F. Bombarda and L. Qu, Nucl. Fusion **37** (1997) 421.

[21] Y.B.Kim, P.H.Diamond and R.J.Groebner, Phys. Fluids B **3** (1991) 2050.

[22] S.Suckewer, H.P. Eubank, R.J. Goldston et al., Nucl. Fusion **21** (1981) 1301.

[23] S.Yamamoto, M. Maeno, S. Sengoku et al., in *Plasma Physics and Controlled Nuclear Fusion Research 1982* Proceedings of the 9th International Conference, Baltimore, Vol.1 (IAEA, Vienna 1983) 73.

[24] A.L. Rogister, Phys. Plasmas **6** (1999) 200.

[25] M. Mattioli, R. Giannella, R. Myrnas et al., Nucl. Fusion **35** (1995) 1115.

[26] E. S. Marmar, J. E. Rice and S. L. Allen, Phys Rev. Lett. **45** (1980) 2025.

[27] TFR Group, Phys. Lett. **87A** (1982) 169.

[28] E. S. Marmar, J. E. Rice, J. L. Terry and F. Seguin, Nucl. Fusion **22** (1982) 1567.

[29] TFR Group, Nucl. Fusion **23** (1983) 559.

[30] B.C. Stratton, A.T. Ramsey, F.P. Boody, C.E. Bush, R.J. Fonck, R.J. Groebner, R.A. Hulse, R.K. Richards and J. Schivell, Nucl. Fusion **27** (1987) 1147.

[31] R. Giannella, L. Lauro-Taroni, M. Mattioli et al., Nucl. Fusion **34** (1994) 1185.

[32] M. Mattioli, C. DeMichelis and A.L. Pecquet, Nucl. Fusion **38** (1998) 1629.

[33] R. Hawryluk, S. Suckewer and S. Hirshman, Nucl. Fusion **19** (1979) 607.

[34] G. Fussman, J. Hofmann, G. Janeschitz et al., J. Nucl. Mater. **162** (1989) 14.

[35] K. Ida, R.J. Fonck, S. Sesnic, R.A. Hulse, B. LeBlanc and S.F. Paul, Nucl. Fusion **29** (1989) 231.

[36] M.E. Perry, N.H. Brooks, D.A. Content, R.A. Hulse, M.A. Mahdavi and H.W. Moos, Nucl. Fusion **31** (1991) 1859.

[37] D. Pasini, M. Mattioli, A.W. Edwards et al., Nucl. Fusion **30** (1990) 2049.

[38] D. Pasini, R.Giannella, L.L.Taroni, M.Mattioli, B.Denne-Hinnov, N.Hawkes, G.Magyar and H.Weisen, Plasma Phys. Contr. Fusion **34** (1992) 677.

[39] J.E. Rice, J.L.Terry, J.A. Goetz et al., Phys. Plasmas **4** (1997) 1605.

[40] F. Ryter, et al., in *Controlled Fusion and Plasma Physics* (Proceedings of the 20th European Conference, Lisbon, 1993) Vol.17C, Part 1, European Physical Society, Geneva (1993) 23.

[41] J.A. Snipes, R.S. Granetz, M. Greenwald, *et al.*, Nucl. Fusion **34**, 1039 (1994).

[42] H. Weisen, F. Hofmann, M.J. Dutch et al., Plasma Phys. Contr. Fusion **38** (1996) 1137.

[43] I.H. Hutchinson, R. Boivin, F. Bombarda et al., Phys. Plasmas **1** (1994) 1511.

[44] G. W. Erickson, J. Phys. Chem. Ref. Data **6** (1977) 831.

[45] E.S. Marmar, J.E. Rice, E. Källne, J. Källne and R.E. LaVilla, Phys. Rev. A **33** (1986) 774.

[46] E. Källne, J. Källne, E.S. Marmar and J.E. Rice, Phys. Scr. **31** (1985) 551.

[47] J.E. Rice, F. Bombarda, M.A. Graf, E.S. Marmar and Y. Wang, Rev. Sci. Instrum. **66** (1995) 752.

[48] D. Mossessian, A.E. Hubbard, E.S. Marmar et al., submitted to Plasma Phys. Contr. Fusion (1999)

[49] T. Sunn Pedersen and R.S. Granetz, Rev. Sci. Instrum., **70** (1999) 586.

[50] M. Greenwald, R.L. Boivin, F. Bombarda et al., Nucl. Fusion **37** (1997) 793.

[51] A.E. Hubbard, R.L. Boivin, R.S. Granetz et al., Plasma Phys. Contr. Fusion **40** (1998) 689.

[52] M. Greenwald, R. Boivin, P. Bonoli et al., submitted to Plasma Phys. Contr. Fusion (1999)

[53] M.A. Graf, J.E. Rice, J.L. Terry et al., Rev. Sci. Instrum. **66** (1995) 636.

[54] W.L. Acton, J.L. Culhane, A.H. Gabriel et al., Ap. J. **244** (1980) L137.

[55] L.A. Vainshtein and U.I. Safronova, Physica Scripta **31** (1985) 519.

[56] L.A. Vainshtein and U.I. Safronova, Atomic Data and Nuclear Data Tables **21** (1978) 49.

[57] R. Mewe and J. Schrijver, Astron. Astrophys. **65** (1978) 99.

[58] R. Mewe, J. Schrijver and J. Sylwester, Astron. Astrophys. **87** (1980) 55.

[59] F. Bely-DuBau, J. DuBau, P. Faucher et al., Mon. Not. R. Astr. Soc. **201** (1982) 1155.

[60] J.H. Irby, E.S. Marmar, E. Sevillano and S.M. Wolfe, Rev. Sci. Instrum. **59** (1988) 1568.

[61] R.A. Hulse, Nucl. Tech./Fus. **3** (1983) 259.

Figure Captions

Fig. 1 Parameter time histories for a 1.1 MA, Ohmic H-mode discharge. In the top frame is the plasma stored energy, in the second frame is the central electron density, in the third frame is the toroidal magnetic field, in the fourth frame is the plasma current and in the fifth frame is the D_α emission. In the bottom frame is the central toroidal rotation velocity of argon ions.

Fig. 2 Comparison of toroidal rotation determined from sawtooth pre- and post-cursors to that of argon ions for an Ohmic H-mode plasma. Also shown are the plasma stored energy and D_α emission. To convert the magnetics rotation frequency to a rotation velocity, multiply by 4.2 m.

Fig. 3 The toroidal rotation velocity increase during the Ohmic H-mode as a function of the plasma stored energy increase, sorted by plasma current. Triangles- 0.8 MA, asterisks- 1.0 MA, dots- 1.2 MA and the box- 1.4 MA.

Fig. 4 The points of Fig.3 with the stored energy normalized to the plasma current.

Fig. 5 The edge electron density profiles during L-mode (dash-dot-dot-dot) and H-mode (solid) are shown in the top frame and the edge electron temperature profiles are shown in the bottom frame, for the discharge of Fig.1. The location of the separatrix is indicated by the dotted vertical line.

Fig. 6 The observed x-ray spectrum of Ca^{18+} (w, x, y and z) and satellites (t, q, r, k, j and 3) is shown by the thick line with the simulation shown by the thin line.

Fig. 7 The brightness time histories of the Ca^{18+} emission following a CaF_2 injection at 0.75 s are shown by the asterisks and the thin solid line. The simulated time history for L-mode (H-mode) is shown by the thick solid (dash-dot-dot-dot) line.

Fig. 8 The impurity diffusion coefficient (top frame) and inward convection velocity (bottom frame) profiles used in the H-mode transport simulations are shown by the solid lines. The calculated neo-classical profiles are shown for comparison by the dash-dot-dot-dot lines.

Fig. 9 The edge x-ray emissivity pedestal is shown by the triangles and the electron density profile (dash-dot-dot-dot line) from Fig.5 is included for comparison. The x-ray emission is modelled by the solid line, which is the product of the electron density and the (calculated) fully stripped F^{9+} density profile. The location of the LCFS is depicted by the vertical dotted line.

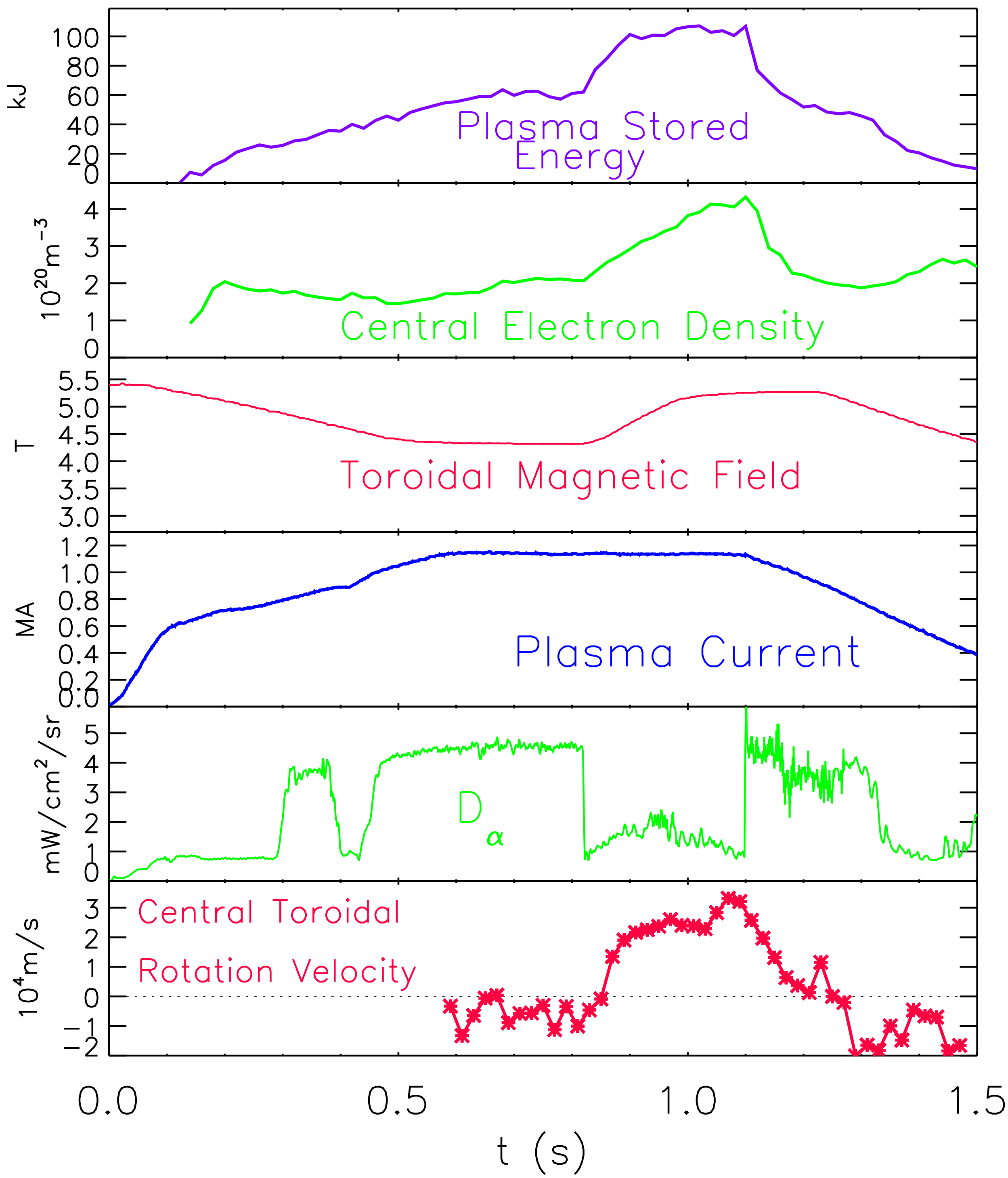

kJ
100
80
60
40
20
0
Plasma Stored
Energy
$10^{20}m^{-3}$
4
3
2
1
0
Central Electron Density
T
5.5
5.0
4.5
4.0
3.5
3.0
Toroidal Magnetic Field
MA
1.2
1.0
0.8
0.6
0.4
0.2
0.0
Plasma Current
$mW/cm^2/sr$
5
4
3
2
1
0
D_α
$10^4m/s$
3
2
1
0
−1
−2
Central Toroidal
Rotation Velocity
0.0
0.5
1.0
1.5
t (s)

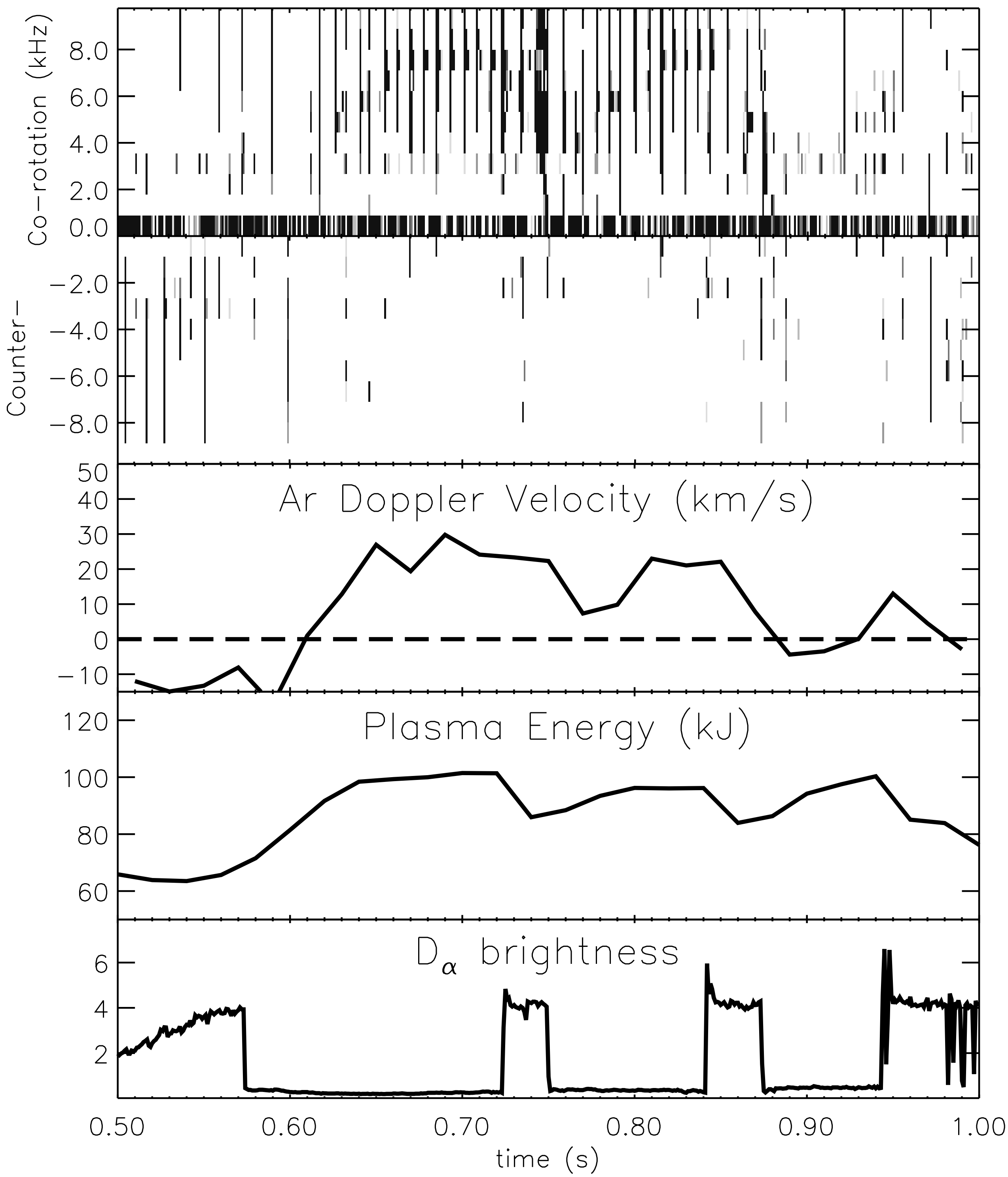

Co-rotation (kHz)
Counter-
8.0
6.0
4.0
2.0
0.0
−2.0
−4.0
−6.0
−8.0
Ar Doppler Velocity (km/s)
50
40
30
20
10
0
−10
Plasma Energy (kJ)
120
100
80
60
D_α brightness
6
4
2
0.50
0.60
0.70
0.80
0.90
1.00
time (s)

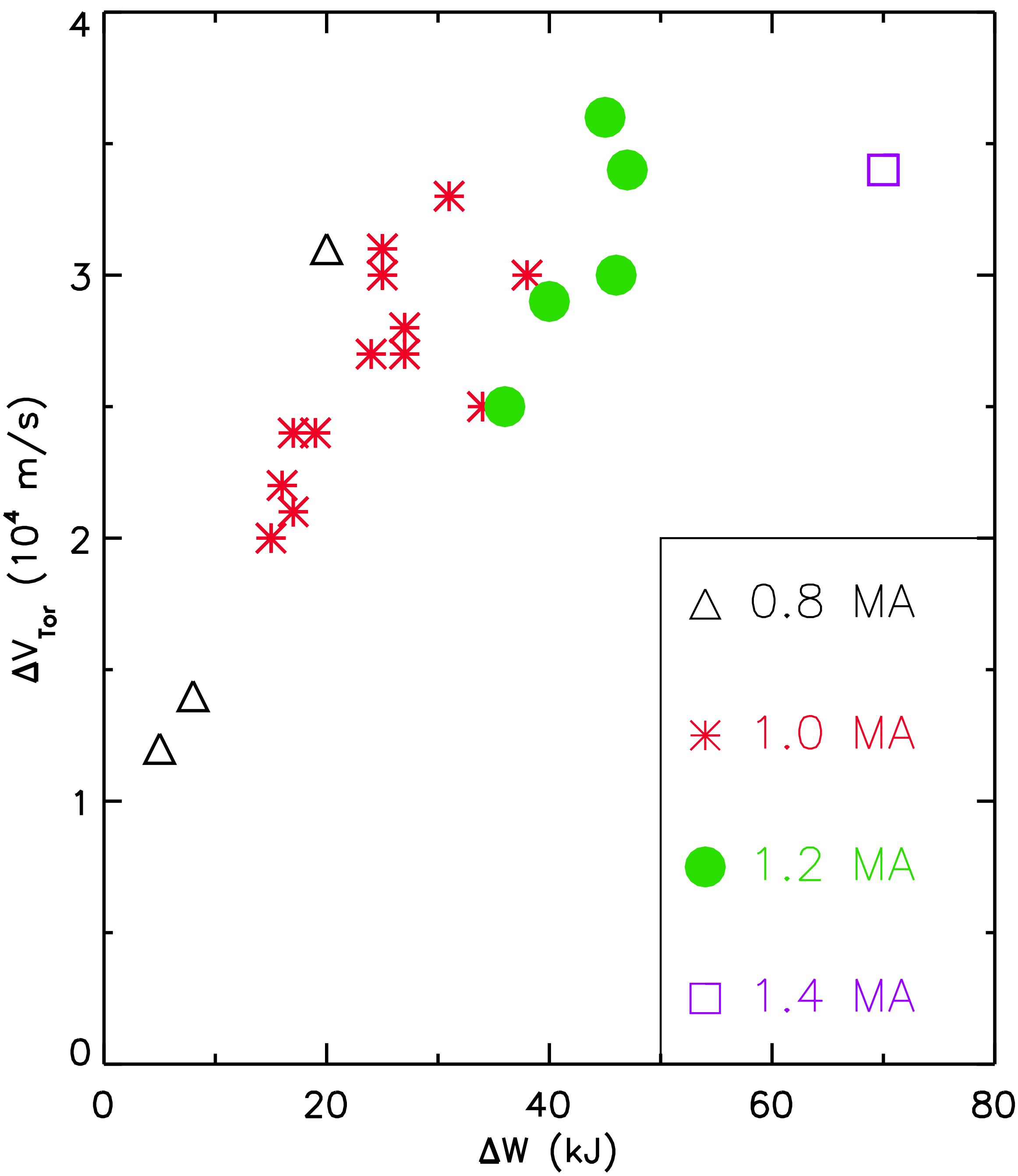

4
3
2
1
0
0
20
40
60
80
ΔW (kJ)
ΔV_Tor (10^4 m/s)
0.8 MA
1.0 MA
1.2 MA
1.4 MA

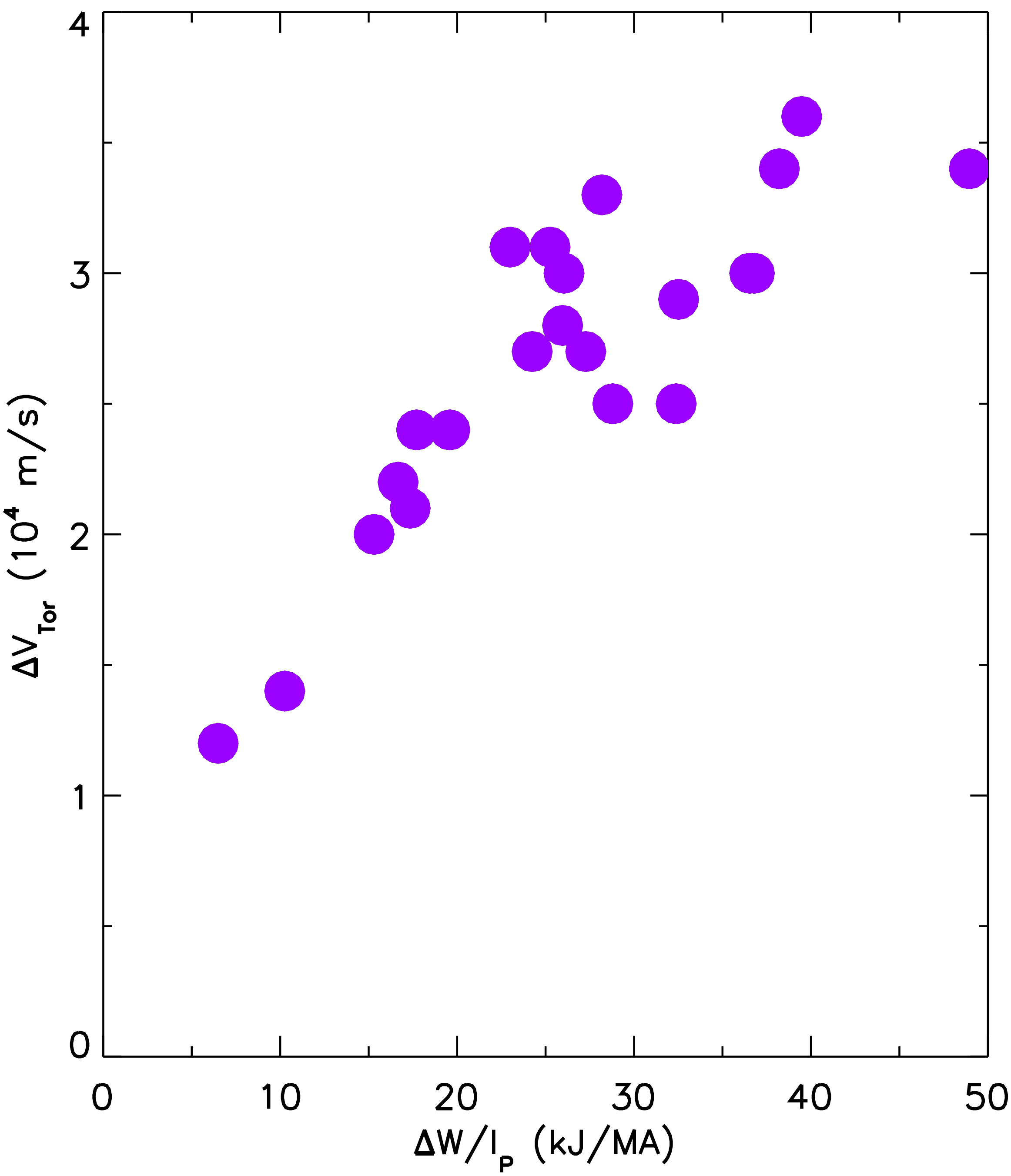

4
3
2
1
0
0
10
20
30
40
50
ΔV_Tor (10^4 m/s)
ΔW/I_P (kJ/MA)

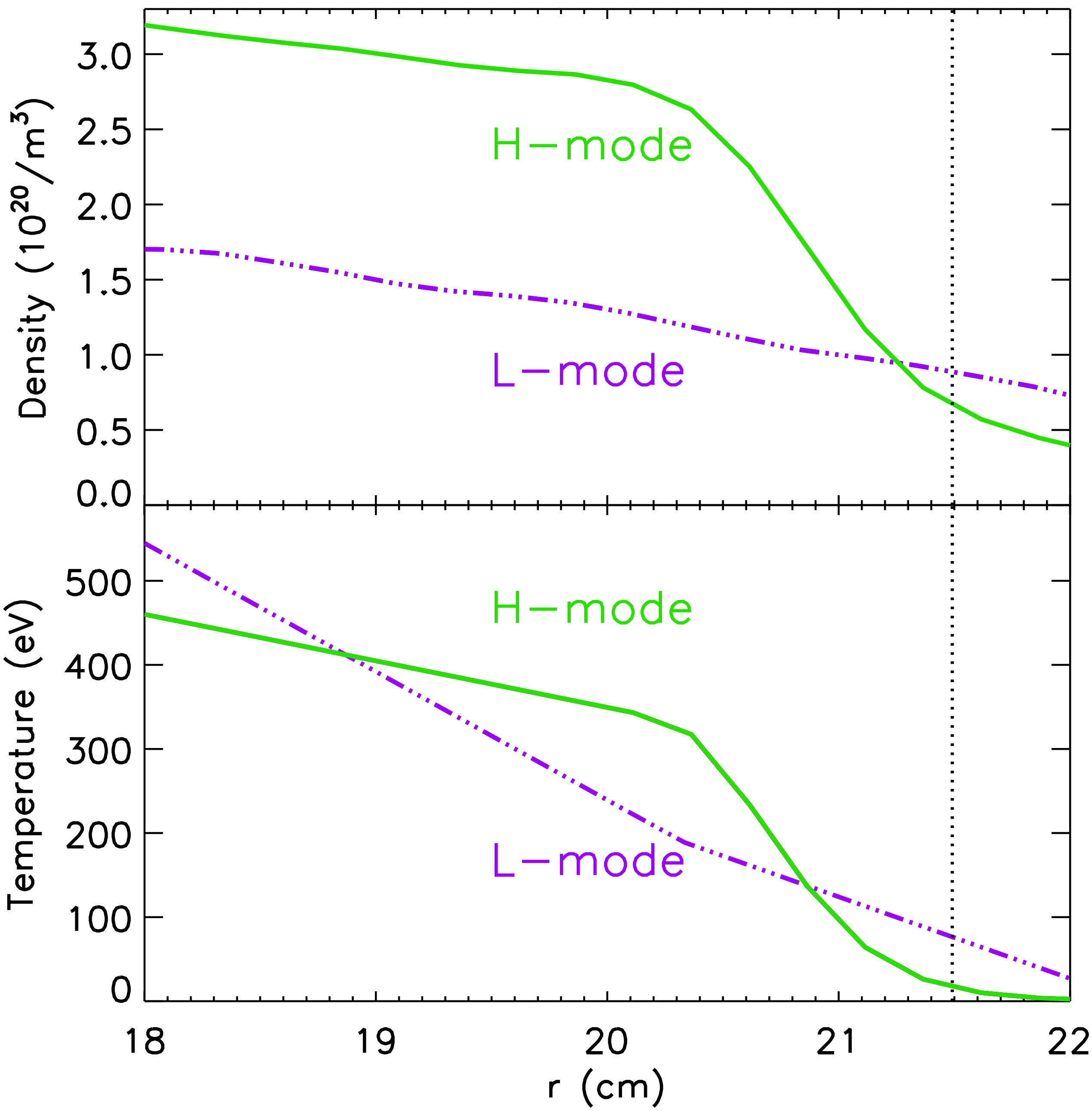

Density (10^20/m^3)
3.0
2.5
2.0
1.5
1.0
0.5
0.0
H-mode
L-mode
Temperature (eV)
500
400
300
200
100
0
H-mode
L-mode
18
19
20
21
22
r (cm)

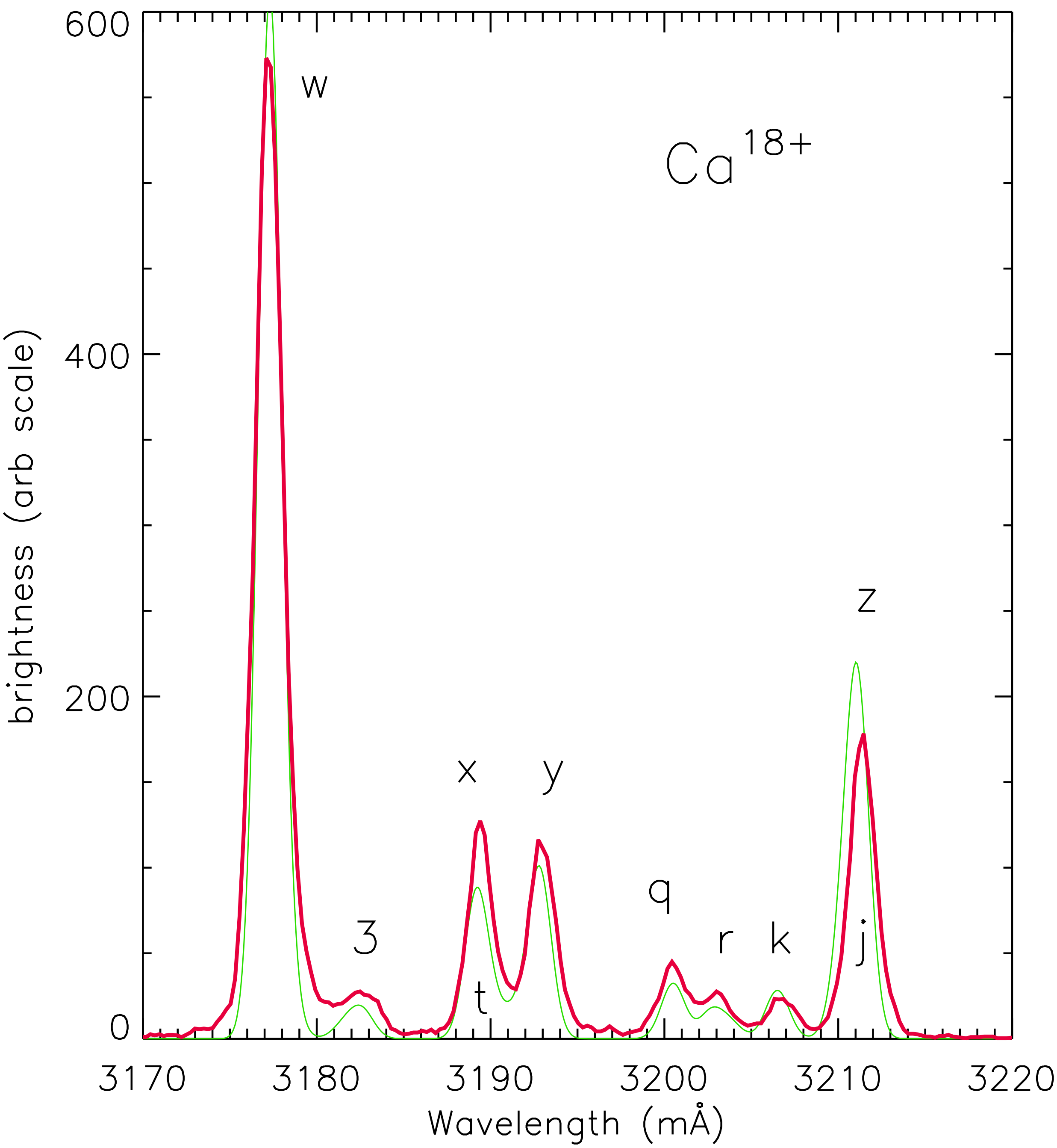

600
400
200
0
brightness (arb scale)
3170
3180
3190
3200
3210
3220
Wavelength (mÅ)
Ca^{18+}
w
3
x
t
y
q
r
k
z
j

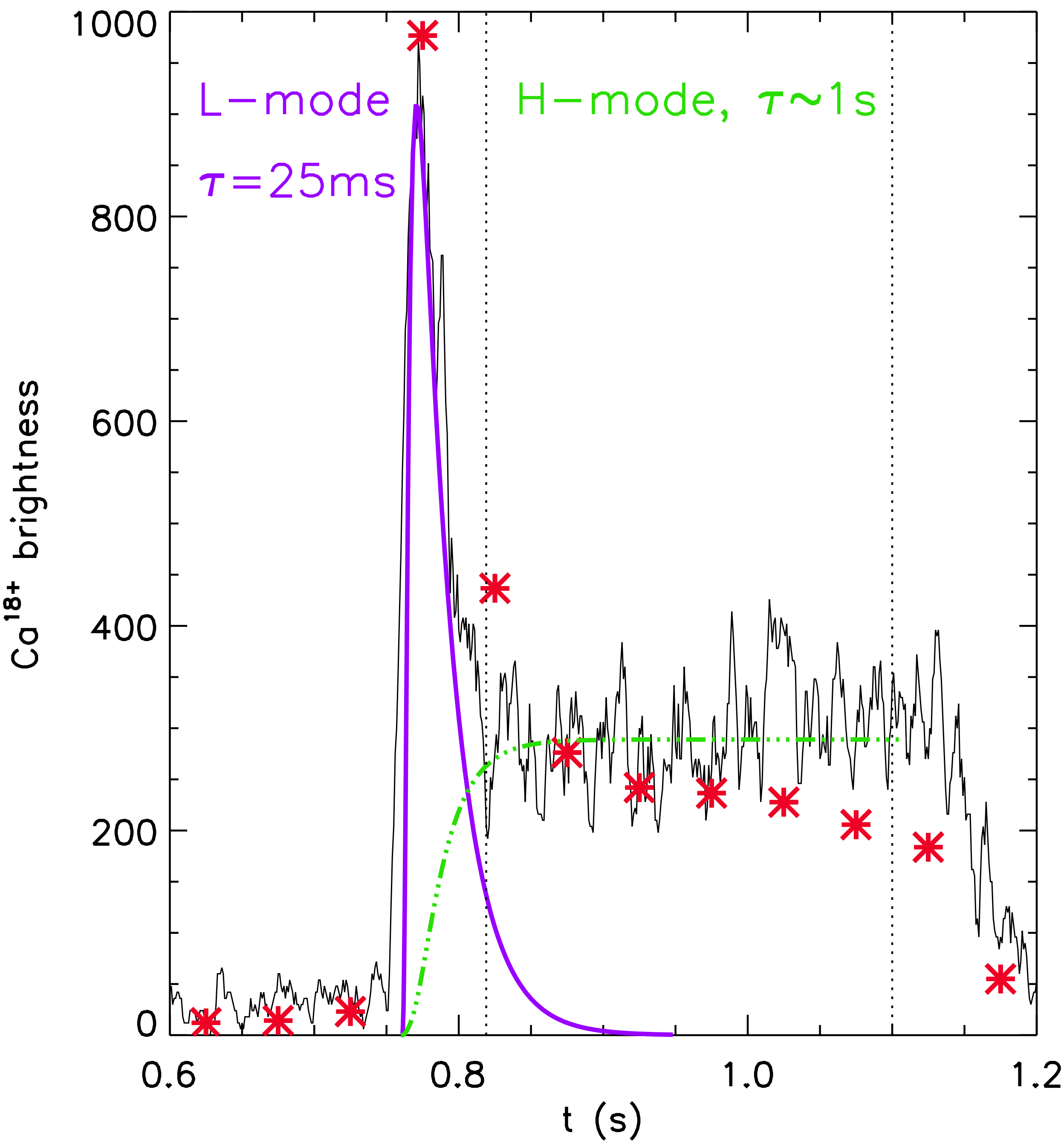

L−mode
τ=25ms
H−mode, τ~1s
1000
800
600
400
200
0
0.6
0.8
1.0
1.2
t (s)
Ca^{18+} brightness

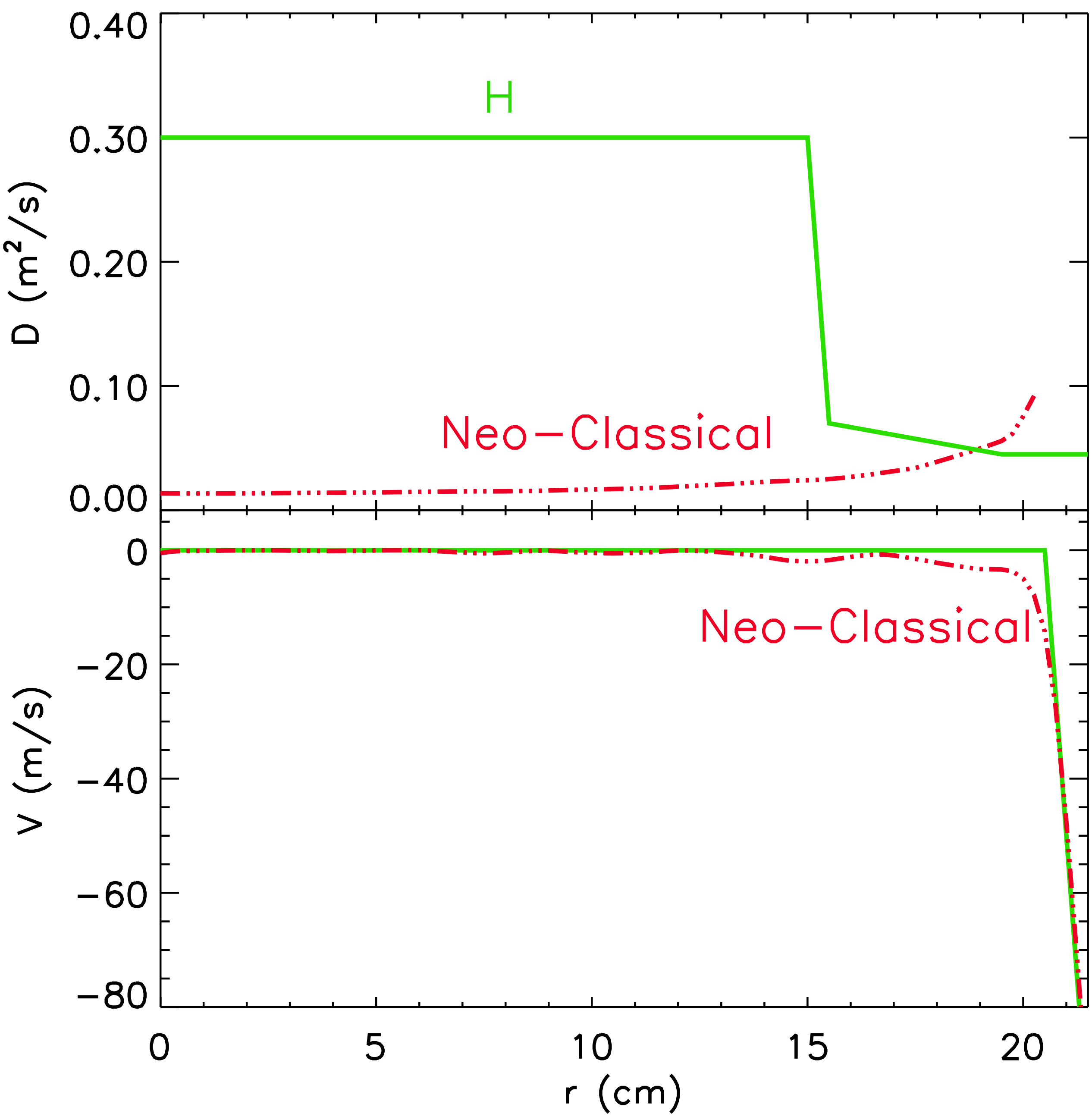

0.40
0.30
0.20
0.10
0.00
D (m²/s)
H
Neo−Classical
0
−20
−40
−60
−80
V (m/s)
Neo−Classical
0
5
10
15
20
r (cm)

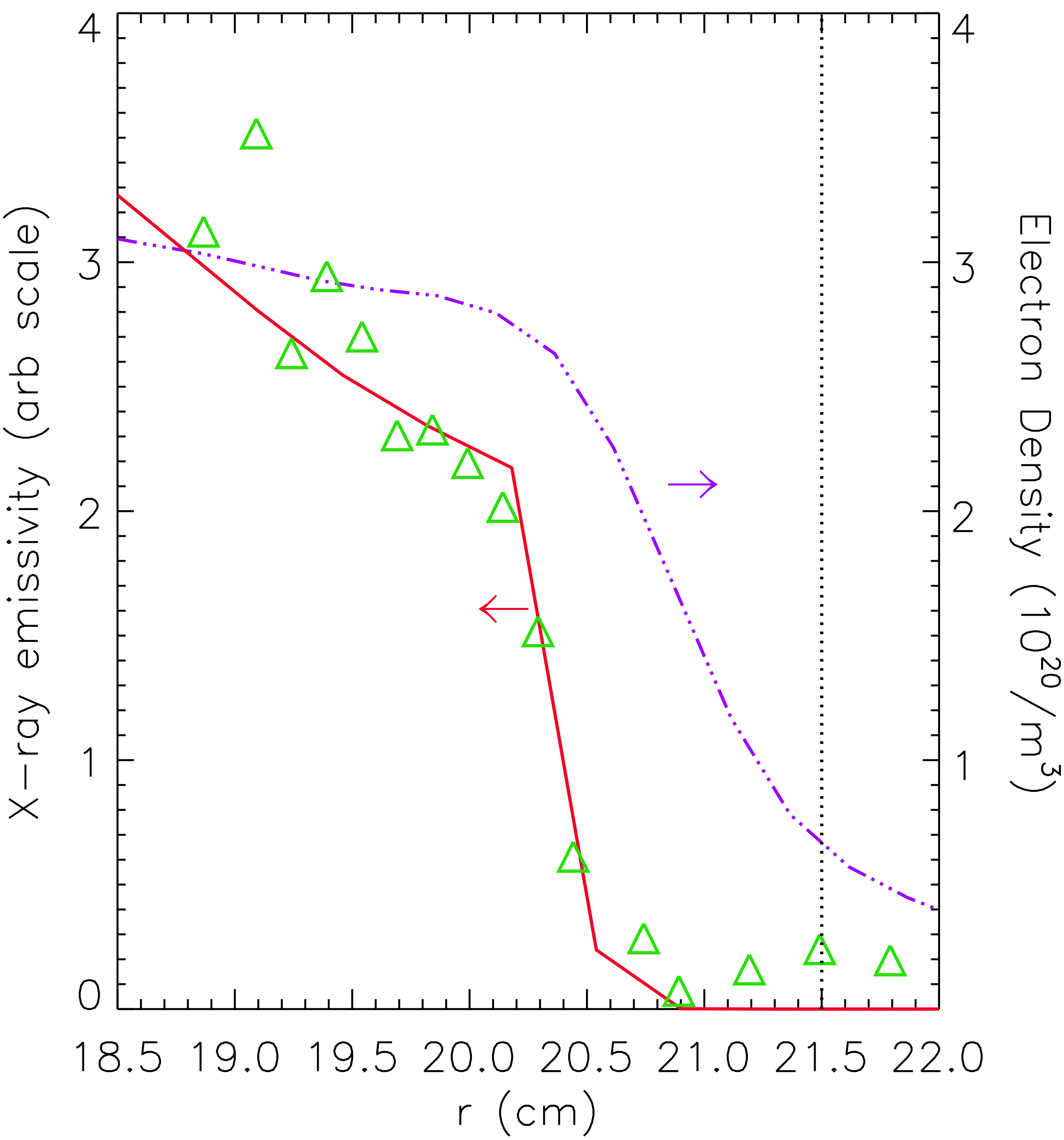
X−ray emissivity (arb scale)
Electron Density (10^20/m^3)
r (cm)
18.5 19.0 19.5 20.0 20.5 21.0 21.5 22.0
0 1 2 3 4